Showcasing collaborative research from Professor Sang-Hee Ko Park's Soft & Smart Materials & Devices laboratory, Department of Material Sciences and Engineering, and Professor Yong-Hoon Cho's Quantum & Nanobio Photonics Laboratory, Department of Physics, Korea Advanced Institute of Science and Technology (KAIST), Daejeon, Republic of Korea.

Active-matrix micro-light-emitting diode displays driven by monolithically integrated dual-gate oxide thin-film transistors

A monolithic low-temperature fabrication process was employed to integrate a-IGZO dual-gate thin-film transistor with GaN-based micro-light-emitting diode (micro-LED) to improve its stability. This process exhibited excellent device performance uniformity and reproducibility, showing promise for ultra-high-resolution displays for augmented and virtual realities and biomedical applications.

As featured in:

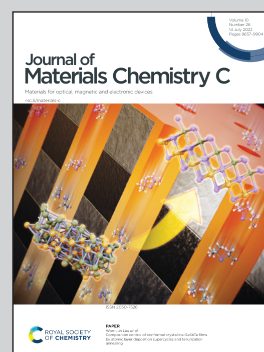

See Yong-Hoon Cho, Sang-Hee Ko Park *et al.*, *J. Mater. Chem. C*, 2022, **10**, 9699.

ROYAL SOCIETY OF CHEMISTRY

rsc.li/materials-c

Registered charity number: 207890

Journal of
Materials Chemistry C

ROYAL SOCIETY
OF CHEMISTRY

PAPER

View Article Online
View Journal | View Issue

Cite this: J. Mater. Chem. C, 2022, 10, 9699

Open Access Article. Published on 27 June 2022. Downloaded on 2/20/2025 2:05:01 PM.
This article is licensed under a Creative Commons Attribution-NonCommercial 3.0 Unported Licence.

Active-matrix micro-light-emitting diode displays driven by monolithically integrated dual-gate oxide thin-film transistors†

Junghoon Yang, ‡[a] HyunWoo Park, ‡[a] Baul Kim, [b] Yong-Hoon Cho *[b] and Sang-Hee Ko Park *[a]

We demonstrate a reliable monolithic process to fabricate micro-light-emitting diodes (μLEDs) driven by highly stable dual-gate structured amorphous indium gallium zinc oxide (a-IGZO) thin-film transistor (TFT) arrays. In contrast to the conventional μLED integration technologies that require the mass transfer of LEDs, our unique monolithic fabrication of oxide TFTs on the GaN epitaxial layer can be applied for accurate integration compared to the method of mounting discrete μLEDs on a backplane individually. To evaluate the applicability of the method at the wafer level, we introduced an atomic-layer-deposited Al_2O_3 insulator film and a denser oxide semiconductor in a dual-gate structured TFT. The induction of controlled hydrogen diffusion from the gate insulator into the active layer at low temperatures led to the good performance of the dual-gate bottom-contact (DGBC) a-IGZO TFTs under positive bias temperature stress (PBTS), negative bias illumination stress (NBIS), and negative bias temperature illumination stress (NBTIS). Monolithic integration of such μLEDs and DGBC a-IGZO TFT arrays was achieved using an organic interlayer dielectric at a low temperature below 230 °C. This simple process exhibits excellent TFT manufacturability (stable V_{on} = 0.78 V), stability (ΔV_{on}, PBTS: 0.03 V, NBIS: −1.85 V, and NBTIS: −3.27 V), uniformity, and reproducibility (less than 4% difference in V_{on}). It shows promise for the mass production of μLED displays for flexible and/or ultra-high-resolution displays for augmented and virtual reality and biomedical applications.

Received 9th May 2022,
Accepted 14th June 2022

DOI: 10.1039/d2tc01905a

rsc.li/materials-c

1 Introduction

Micro-light-emitting diodes (μLEDs) are promising as next-generation displays for application in augmented reality (AR) owing to their high luminous efficiency, rapid response time, high stability, and low power consumption as compared to liquid crystal and organic LED displays.[1–7] Furthermore, there is a growing demand for ultra-high-resolution mobile displays for virtual reality (VR) and AR active-matrix μLEDs to become thinner and more lightweight while maintaining a high pixel density.[8] Possible driving devices for the active-matrix μLED array include complementary metal–oxide–semiconductor field-effect transistors (MOSFETs) and thin-film transistors (TFTs).[9–12] Although traditional Si-based MOSFETs have been widely used because of their high package density, high readout speed, and low noise,[13,14] the high fabrication cost and rigidity limit their application.[15] Conversely, the TFT backplane offers several advantages such as a large-area process, flexibility, excellent performance, and low cost.[16]

Among the various TFT backplanes, low-temperature polycrystalline silicon (LTPS) TFTs have been used in driving high-resolution μLEDs. Recently, Kim *et al.* developed remarkably bright active-matrix μLEDs using the LTPS TFT backplane.[17] A solder bump material was employed for bonding the LTPS backplane to the μLED array. However, this process may cause pressure damage and stress within the μLEDs, which results in a fracture.[18] Others have successfully developed a 12.1 inch 169 ppi full-color μLED display by transferring μLEDs to the LTPS TFT backplane.[19] Despite their careful integration, LTPS TFTs have inherent drawbacks in terms of power consumption and high costs.[20,21] In contrast, amorphous oxide semiconductor TFTs with high mobility, stability, and uniformity can also drive μLEDs with a high pixel density.[22,23] Recently, Sun *et al.* developed a 4 inch full-color μLED display based on indium gallium zinc oxide (IGZO) TFTs.[24] The mass transfer was used

[a] *Department of Materials Science and Engineering, Korea Advanced Institute of Science and Technology (KAIST), 291 Daehak-ro, Yuseong-gu, Daejeon 34141, Republic of Korea. E-mail: shkp@kaist.ac.kr*
[b] *Department of Physics and KI for the NanoCentury, Korea Advanced Institute of Science and Technology (KAIST), 291 Daehak-ro, Yuseong-gu, Daejeon 34141, Republic of Korea. E-mail: yhc@kaist.ac.kr*

† Electronic supplementary information (ESI) available. See DOI: https://doi.org/10.1039/d2tc01905a

‡ These authors contributed equally.

Open Access Article. Published on 27 June 2022. Downloaded on 2/20/2025 2:05:01 PM.
This article is licensed under a Creative Commons Attribution-NonCommercial 3.0 Unported Licence.

to integrate more than 170 000 flip-chip RGB μLEDs on the IGZO TFT backplane. However, the transfer of LEDs is associated with yield issues, and the mass transfer is not yet commercially viable, particularly for a high-resolution display with a small pixel pitch. Additionally, a lower yield during transfer significantly affects the performance of the μLED display. Therefore, it is necessary to integrate the TFT array monolithically into the μLED array.

However, this limits the process temperature for the oxide TFT array because the planarization of the μLED array is achieved by a photo-patternable organic polymer. Therefore, oxide TFT arrays should be fabricated on top of the μLED array at a low temperature in order to secure the properties of the planarization material. In general, the defects in the oxide semiconductor and/or the interface between the active layer and the gate insulator (GI) can be minimized by semiconductor densification and defect passivation during the annealing process over 300 °C.[25–28] Moreover, the instability of oxide TFTs under electrical bias, light, and temperature is a critical hurdle against the commercialization of current driven displays such as μLEDs. Based on this viewpoint, it is essential to develop a highly reliable oxide TFT on a μLED array at low temperatures for monolithic integration.

Herein, we describe the first monolithic fabrication of amorphous (a)-IGZO TFTs on a GaN-based μLED array. Our fabrication method could be achieved by introducing an a-IGZO channel with a high film density and atomic-layer-deposited dielectric layers in a dual-gate TFT structure to eliminate the charge trapping defects within the active bulk and/or the interface between the active layer and GI. In addition, the opaque bottom gate of our dual-gate TFT can block the light of top-emission μLEDs, securing the light stability of a-IGZO TFTs during the operation. Through this process, we obtained highly stable a-IGZO TFTs under positive bias temperature stress (PBTS), negative bias illumination stress (NBIS), and negative bias temperature illumination stress (NBTIS) environments. We demonstrated the excellent stability of low-temperature a-IGZO TFTs and its correlation with defects through various thin-film analyses. On the basis of these characteristics, it has been verified that a multigate transistor is also capable of performing reliable logic and synopsis operations by controlling the gate voltage.[29] This unique monolithic fabrication method of the oxide TFT array provides the groundwork for fabricating large-area, high-resolution, and highly stable μLED displays at low cost.

2 Experimental

2.1 Preparation of pixelated μLED arrays

Fig. 1 shows a schematic image of the monolithic dual-gate a-IGZO TFT and materials for each layer. The growth and fabrication of GaN-based blue μLEDs were conducted as follows: the 1.5 μm-thick undoped GaN, 2.4 μm-thick n-type GaN, 250 nm-thick InGaN/GaN superlattice, 50 nm-thick InGaN/GaN multi-quantum well, 30 nm-thick AlGaN electron-blocking

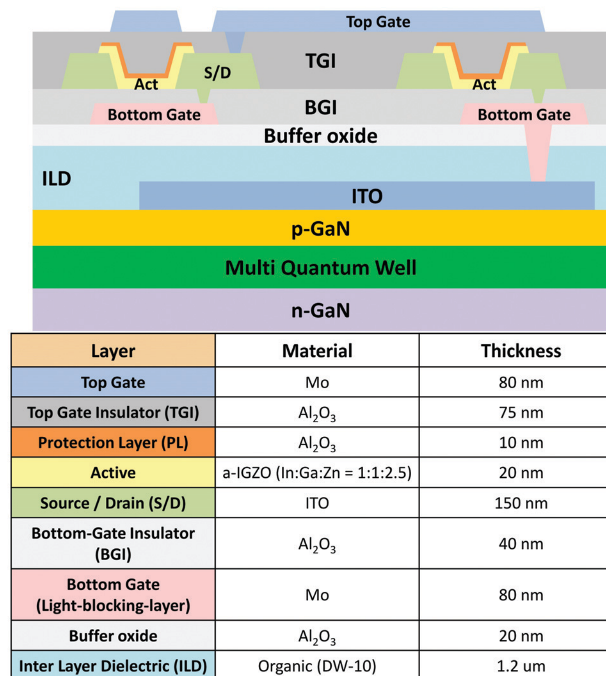

Layer	Material	Thickness
Top Gate	Mo	80 nm
Top Gate Insulator (TGI)	Al_2O_3	75 nm
Protection Layer (PL)	Al_2O_3	10 nm
Active	a-IGZO (In:Ga:Zn = 1:1:2.5)	20 nm
Source / Drain (S/D)	ITO	150 nm
Bottom-Gate Insulator (BGI)	Al_2O_3	40 nm
Bottom Gate (Light-blocking-layer)	Mo	80 nm
Buffer oxide	Al_2O_3	20 nm
Inter Layer Dielectric (ILD)	Organic (DW-10)	1.2 um

Fig. 1 A schematic image of a monolithic dual-gate amorphous indium gallium zinc oxide (a-IGZO) thin-film transistor (TFT) and materials for each layer.

layer, and 250 nm-thick p-GaN were epitaxially grown on sapphire substrates *via* metal–organic chemical vapor deposition. The blue LEDs were pixelated by inductively coupled plasma-reactive ion etching. Next, 100 nm-thick indium-tin oxide (ITO) as the electron spread layer was deposited using an e-beam evaporator and subjected to rapid thermal annealing. The remaining layers were coated with an organic interlayer dielectric (ILD; DW-10; a negative photoresist) to ensure smooth surface morphology and planarization. The organic ILD was patterned to create holes that facilitated the subsequent connection with the a-IGZO TFT arrays.

2.2 Fabrication of the dual-gate bottom-contact (DGBC) a-IGZO TFT array on the planarized μLED arrays

A 20 nm-thick Al_2O_3 buffer oxide layer was deposited *via* thermal atomic layer deposition (T-ALD) using the tri-methyl aluminum (TMA) precursor and water at 150 °C on the planarization layer to ensure that water and hydrogen from the ILD could not reach a-IGZO TFTs. The bottom gate (80 nm-thick Mo), also acting as a light-blocking layer, was deposited *via* direct current (DC) sputtering at 5 mTorr and 200 W. The light-blocking layer was photoetched. A 40 nm-thick Al_2O_3 bottom-gate insulator (BGI) was deposited *via* T-ALD using TMA and water at 150 °C. The BGI was then etched (using the buffer oxide etchant, BOE) in order to expose the electrode. Subsequently, a 150 nm-thick ITO source/drain (S/D) electrode was deposited *via* DC sputtering. Heat treatment at 230 °C for 2 h *in vacuo* was performed to ensure a uniform clean-etch profile. The ITO film was patterned using a poly-ITO etchant. A 20 nm-thick a-IGZO layer was deposited *via* radiofrequency sputtering

 This journal is © The Royal Society of Chemistry 2022

Open Access Article. Published on 27 June 2022. Downloaded on 2/20/2025 2:05:01 PM.
This article is licensed under a Creative Commons Attribution-NonCommercial 3.0 Unported Licence.

at room temperature (15 to 25 °C), with a partial pressure of 30% P_{O2} and 70% P_{Ar} at 0.075 Pa; the metal cation ratio was 1 : 1 : 2.5 (In : Ga : Zn).[30] A 10 nm-thick-Al_2O_3 protection layer (PL), which suppresses the formation of defects within the active layer during the patterning process,[31] was deposited at 150 °C *via* T-ALD using water as the oxidant. The a-IGZO layer and PL were simultaneously patterned using 49% (v/v) HF diluted in 100 : 1. The top gate insulator (TGI) of the 75 nm-thick Al_2O_3 layer was deposited at 150 °C *via* T-ALD and patterned using BOE. The 80 nm-thick Mo top gate electrode was deposited *via* DC sputtering under 5 mTorr of Ar at 200 W. The Mo layer was patterned *via* wet etching. Finally, the device was heat-treated for 2 h *in vacuo* at 230 °C. The subpixels of the fabricated monolithic μLEDs were observed *via* focused ion beam scanning electron microscopy (FIB-SEM; Helios Nanolab 600).

2.3 Electrical characterization

Transfer and output curves were obtained using an HP4156A analyzer; the relevant parameters were extracted from the transfer curves. The measured channel width/length of all TFTs was 20 μm/20 μm. The gate voltage sweep range for the transfer curves was −15 to 20 V, in steps of 250 mV. The drain voltages were 0.1 and 10 V, and the drain voltage sweep range for the output curve was −2 V to 20 V, in steps of 500 mV. The gate voltage range was −5 to 20 V, in steps of 5 V. The TFT PBTS transfer curves were obtained at a voltage stress of 1 MV cm^{-1} and a temperature stress of 60 °C over 10 000 s. The TFT NBIS transfer curves were obtained at a voltage stress of 1 MV cm^{-1} under a white light stress of 0.5 mW cm^{-2} over 10 000 s. The TFT NBTIS transfer curves were obtained at a voltage stress of 1 MV cm^{-1}, a temperature stress of 60 °C, and a white light stress of 0.5 mW cm^{-2} over 10 000 s. The device was operated under ambient environmental conditions (27.5 °C, 34% humidity).

3 Results and discussion

In this paper, the performance of a-IGZO TFTs including both top-gate bottom-contact (TGBC) and DGBC architectures was evaluated, in which T-ALD Al_2O_3 and sputtered Mo were adopted as the dielectric and gate layers, respectively. Both structures of TFTs were fabricated on top of the μLED array, which was formed on a sapphire substrate. More importantly, it is essential to minimize the charge trapping defect such as oxygen interstitials (O_i) and maximize the density of the oxide semiconductor film to obtain highly stable a-IGZO TFTs in the low-temperature process.[32] In particular, the film density of an active layer significantly changes according to the post-annealing process.[33] This change in density is mainly attributed to the structural relaxation or rearrangement of the matrix by thermal energy.[34] Therefore, we evaluated the morphology and density of the a-IGZO active layers annealed at different temperatures. As shown in Fig. S1 (ESI†), atomic force microscopy revealed no significant effect of annealing temperature on the surface roughness of the a-IGZO thin films. For a detailed analysis, we subjected the samples to X-ray reflectometry (XRR) to explore the density of the thin films. The density of the a-IGZO thin films was obtained from the critical angle (θ_c) of the XRR curve, where reflectivity decreased rapidly. Thus, the difference in the density values was only 0.035 g cm^{-3} between an as-fabricated sample and a 300 °C annealed sample (Fig. S2, ESI†). These results reveal that our a-IGZO films have a sufficient film density without additional heat treatment after the deposition. Because the sputtering pressure was very low at 0.075 Pa during the deposition, we could obtain an a-IGZO thin film with sufficient density and roughness in a pristine state.[35] Thus, these a-IGZO films deposited at low pressure can be applied to fabricate a highly stable oxide TFT even at a low temperature.

Subsequently, we investigated the effect of the active layer/insulator interface on electrical properties. Generally, it is crucial to control the defects within the active layer itself and the interface traps between the active layer and GI for the excellent reliability of oxide TFTs.[36,37] We fabricated TGBC TFTs with stack structures similar to those of self-aligned TFTs, which are advantageous for large-sized and high-resolution displays.[38] Additionally, we applied the ALD-Al_2O_3 insulator film to both PLs and GIs because of its high quality even when deposited at a low temperature.[39,40] The details of the fabrication method of TGBC TFTs are described in the ESI.† To identify the optimized characteristics of TFTs in terms of V_{on}, mobility, and stability, we fabricated TGBC a-IGZO TFTs by applying two different Al_2O_3 deposition methods [T-ALD and plasma-enhanced ALD (PE-ALD)] to the PL and GI. Initially, we fabricated each pair of TGBC TFTs to determine the suitable deposition method for the monolithic TFT fabrication. All four samples were annealed *in vacuo* at 230 °C for 2 h.

Fig. 2(a–d) show the transfer curves of a-IGZO TGBC TFTs at drain voltages of 0.1 and 10 V prepared using (a) T-ALD/T-ALD, (b) PE-ALD/T-ALD, (c) T-ALD/PE-ALD, and (d) PE-ALD/PE-ALD for PL/GI deposition. We used a thin PL (first GI) to protect the active a-IGZO layer because the 1 : 1 : 2.5 ratio of the a-IGZO film is vulnerable to the acid during the etching process.[41] Fig. 2(e) illustrates that the hysteresis of each TFT [(a–d)] is 0.25, 5.75, 0.75, and 16.5 V, and the linear mobilities are 20.31, 4.47, 25.31, and 0.97 cm^2 V^{-1} s^{-1}, respectively. When PE-ALD PLs were used, the hysteresis was higher and the linear mobility was lower than those of TFTs adopting T-ALD PLs. While the PE-ALD process suppressed the generation of the shallow donor of oxygen vacancies in the active layer, it yielded charge trapping centers in both the active layer and the interface between the active layer and the GI compared with T-ALD.[42] These differences are ascribed to two different oxidants: water and oxygen plasma. Oxygen plasma collisions create O_i-related states, which act as electron acceptor-like traps, thereby decreasing the electron mobility and increasing the hysteresis by capturing free electrons in the a-IGZO active layer and/or the interface between the active layer and GI.[43,44] The transfer characteristics of TFTs using the PE-ALD method represented a higher hysteresis compared to the T-ALD method. Furthermore, the Al_2O_3 film deposited by PEALD did not contain enough H to be

Open Access Article. Published on 27 June 2022. Downloaded on 2/20/2025 2:05:01 PM.
This article is licensed under a Creative Commons Attribution-NonCommercial 3.0 Unported Licence.

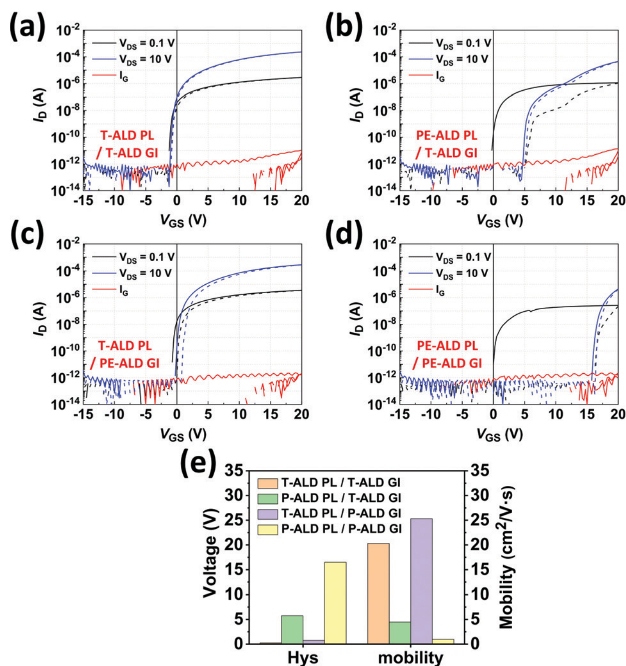

Fig. 2 Transfer curves of a-IGZO TGBC TFTs prepared using (a) T-ALD/T-ALD, (b) PE-ALD/T-ALD, (c) T-ALD/PE-ALD, and (d) PE-ALD/PE-ALD for PL/GI Al_2O_3 deposition. (e) Hysteresis and linear mobility values of various a-IGZO TFTs.

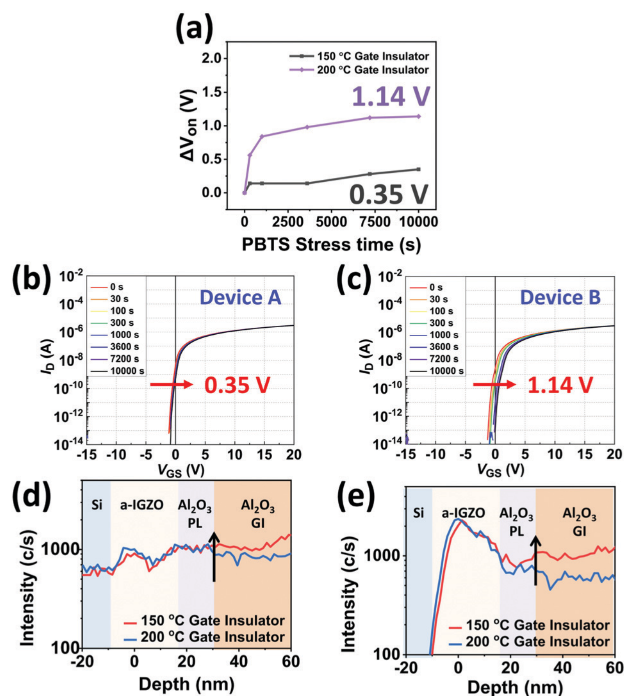

Fig. 3 (a) V_{on} shifts according to the GI growth temperature. PBTS stability of TGBC a-IGZO TFTs with GI Al_2O_3 deposited at (b) 150 °C and (c) 200 °C. (d) Hydrogen and (e) hydroxyl group peaks dictated from SIMS analysis.

diffused from the active layer into the GI. This can leave the charge trapping centers generated by oxygen plasma incompletely passivated, yielding hysteresis [Fig. 2(b–d)]. Conversely, the device that applied the T-ALD-Al_2O_3 insulator film to both the GI and PL showed the best electrical performance by suppressing the formation of charge trapping centers at the active/insulator interface [Fig. 2(a)].[45] Therefore, we concluded that using a T-ALD-Al_2O_3 insulator film is preferable for fabricating highly stable oxide TFTs at low temperatures.

The delicate control of the deposition temperature of GI is a crucial factor in securing the high stability of the metal–oxide transistor.[46] For more detailed optimization, we manufactured another TGBC a-IGZO TFT by changing the deposition temperature of GI to 200 °C. Hence, we fabricated a second device (device B, PL: 150 °C and GI: 200 °C) wherein the turn-on voltage was shifted by 1.14 V after the PBTS measurements, which was larger than the shift of the turn-on voltage of device A (0.35 V) [Fig. 3(a)]. According to the secondary-ion mass spectrometry (SIMS) analysis, the amounts of hydrogen and hydroxyl at the PL/GI interface were lower in device B than those in device A [Fig. 3(d and e)]. In general, ALD at a higher growth temperature lowers the amount of residual hydrogen in the films due to the complete removal of the hydroxyl groups during the surface reaction.[46] However, the amount of hydrogen in the active layer/PL interface was similar for devices A and B. Because ALD-Al_2O_3 is an excellent hydrogen barrier,[47] the temperature for the GI deposition on the top of the PL does not affect the TFT instability directly. However, in contrast to the structure of thin films for SIMS analysis, in which a-IGZO was completely covered with the Al_2O_3 PL, the contact between the GI of the TFT and the side edge of the exposed a-IGZO was noticeable despite the presence of the PL. Therefore, hydrogen can diffuse toward the active layer/GI interface *via* these contact areas to affect the reliability. These careful analyses confirmed that the increased hydrogen levels within the PL and GI were associated with improved PBTS stability. Therefore, we selected the structure of device A with good PBTS stability for fabricating monolithic oxide TFTs on the μLED array.

Before fabricating the monolithic μLEDs, we investigated the electrical properties of the a-IGZO TGBC TFTs of device A under various environments (Fig. S3, ESI†). Although the subthreshold swing, turn-on voltage, uniformity, and hysteresis values were excellent, the output characteristics showed that the drain current was not saturated at a high drain voltage. As the current saturation characteristics of TFTs have important effects on driving the μLEDs with constant luminance,[48] the driving TFTs must have a saturation drain current at a specific drain voltage. In addition, the turn-on-voltage shift was −7.07 V during the NBIS stability measurements over 10 000 s at −1 MV cm^{-1} and 0.5 mW cm^{-2} white light stress. Because the NBIS measurement environment corresponds to the major operation state of the μLED display,[49] these unfavorable NBIS characteristics should also be addressed. Generally, the deterioration in NBIS stability originates from hydrogen impurities or ionized oxygen vacancies in metal–oxide semiconductors.[47] In addition, the subgap density-of-states caused by the metal–hydrogen bonds or non-bridging oxygen hole centers can

This journal is © The Royal Society of Chemistry 2022

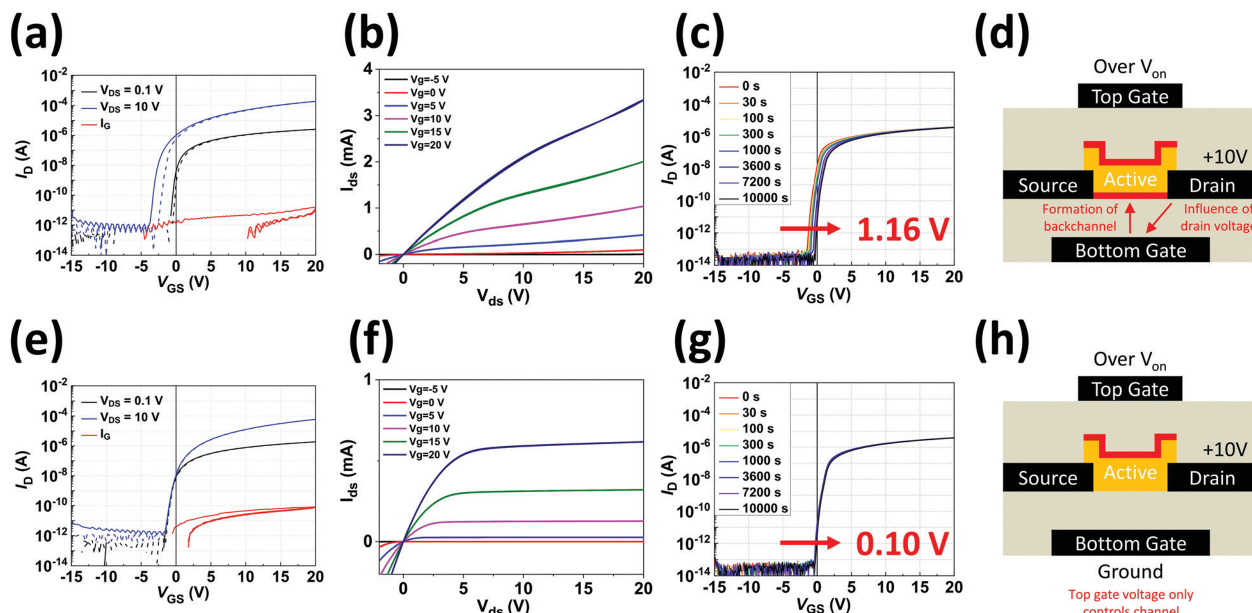

Fig. 4 (a and e) The transfer curve, (b and f) output curve, (c and g) PBTS stability (60 °C, 10 000 s, 1 MV cm^{-1}), and (d and h) schematics of the DGBC a-IGZO TFT in the absence and presence of a ground voltage at the bottom gate, respectively.

Open Access Article. Published on 27 June 2022. Downloaded on 2/20/2025 2:05:01 PM.
This article is licensed under a Creative Commons Attribution-NonCommercial 3.0 Unported Licence.

degrade the stability of NBIS.[49,50] In our results, the NBTIS characteristics were poor compared to those of NBIS due to the trapping of the ionized oxygen vacancies into the defects of Al–OH or Si–OH in the gate insulator by light and thermal stress.[51] Hence, to overcome these drawbacks, we inserted opaque light-blocking layers (Mo bottom gate) in the dual-gate structure.[52]

Fig. 4(a–d) illustrates the results of a DGBC a-IGZO TFT without applying any bottom-gate voltage, while Fig. 4(e–h) shows the corresponding results in the presence of a ground bottom-gate voltage. As shown in Fig. 4, various improved electrical properties were obtained simultaneously after a ground voltage was applied to the bottom gate. First, the ground voltage of the bottom gate rendered the turn-on voltage of the DGBC TFTs consistent regardless of the applied drain voltage [Fig. 4(a and e)]. Second, the saturated drain current was achieved, as identified from the output curves [Fig. 4(b and f)]. Third, the enhanced PBTS characteristics were also obtained; the turn-on-voltage shift during PBTS decreased from 1.16 V to 0.10 V [Fig. 4(c and g)]. These phenomena could be explained by the schematics in Fig. 4(d and h). The V_{on} shift is caused by the electron accumulation or depletion after application of the bottom gate voltage (V_{BG}), in which a negative V_{BG} generates a positive shift and a positive V_{BG} induces a negative shift [Fig. S4, ESI†].[53] This shift can also be affected by introducing impurities serving as carriers, such as hydrogen. However, T-ALD Al_2O_3 used as the buffer oxide plays as an effective barrier, preventing impurities from entering the active interface layer. Therefore, the impact of these impurities can be effectively reduced.[47] In the absence of electrical voltage with the bottom gate, the electric field caused by the drain voltage was transferred to that bottom gate. Thus, a backchannel in the a-IGZO active layer was induced close to the bottom gate. This induced backchannel can shift the turn-on voltage in a negative direction as the drain voltage increases. Furthermore, because the backchannel current can be increased as the drain voltage increases, it is difficult to gain drain saturation current characteristics in an output curve. Simultaneously, from the viewpoint of electrical stability, this backchannel surface serves as a charge trapping site at the active layer/BGI interface, thereby deteriorating the stability of PBTS.[54] In contrast, when the ground voltage is applied to the bottom gate, the problems mentioned above are solved as the channel is formed only in the a-IGZO region close to TGI [Fig. 4(d and h)]. Indeed, the DGBC TFTs exhibited outstanding electrical properties, including low hysteresis, hard-saturation characteristics, and good PBTS stability, when a ground voltage was applied.

The PBTS stability of DGBC a-IGZO TFTs was measured over 10 000 s at 60 °C and 1 MV cm^{-1} according to the BGI deposition temperatures (150 °C, 200 °C, and 300 °C) to clarify the effect of the deposition temperature of the BGI on the electrical reliability (Fig. S5, ESI†). The amount of hydrogen in the GI can improve the PBTS stability by diffusing to the a-IGZO/GI interface. Similarly, the amount of hydrogen in the BGI positively influences the improvement of PBTS stability, supported by the SIMS data (Fig. S5, ESI†). As the deposition temperature of the BGI decreased, more amount of hydrogen was detected in the channel. Consequently, the BGI deposited at low temperatures contained more hydrogen, thereby enhancing the PBTS stability. These results suggest that our BGI films deposited at low temperatures are suitable for fabricating highly stable DGBC TFTs. Thus, high-performance DGBC TFTs can be fabricated using the Al_2O_3 BGI deposited at 150 °C.

To monolithically integrate the optimized DGBC TFTs on the μLED array, a thick photo-patternable insulating layer is required to planarize the pixelated μLEDs. Therefore, an organic ILD (a negative photoresist, DW-10) was introduced,

Open Access Article. Published on 27 June 2022. Downloaded on 2/20/2025 2:05:01 PM.
This article is licensed under a Creative Commons Attribution-NonCommercial 3.0 Unported Licence.

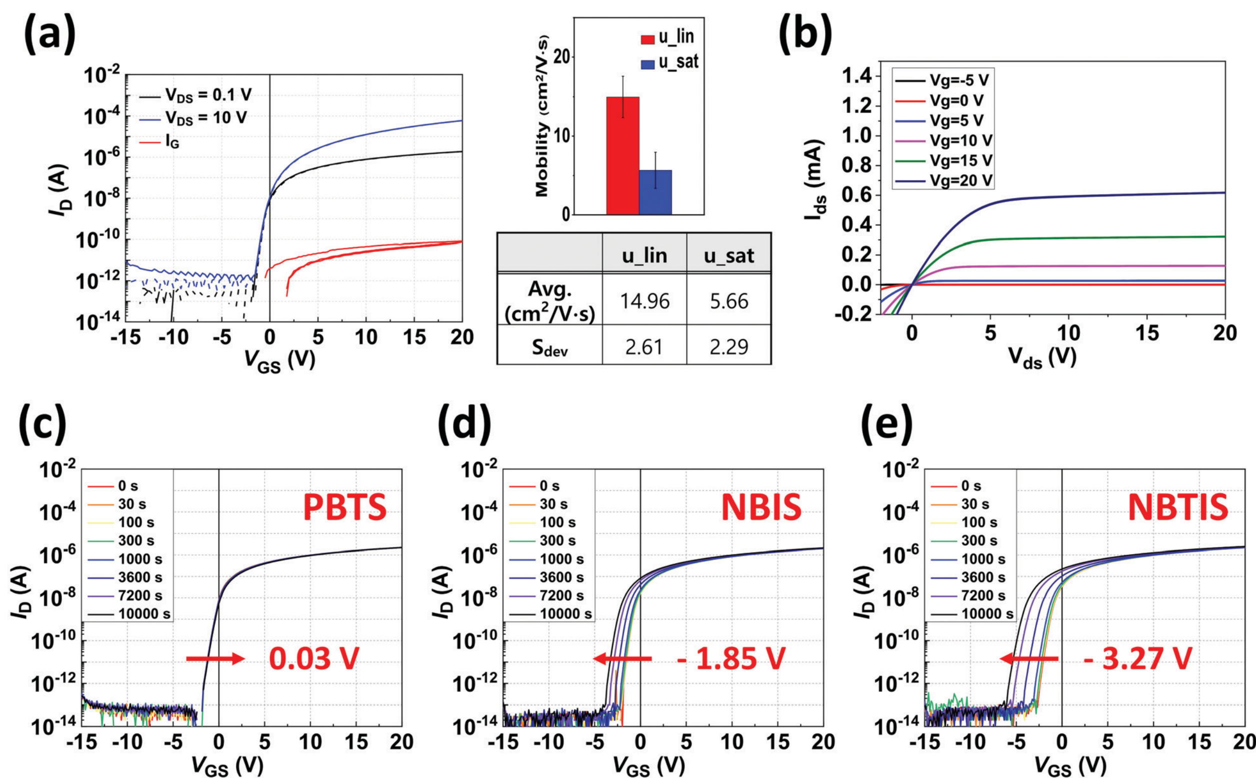

Fig. 5 (a) Transfer curves and mobility parameters, (b) output curves, (c) PBTS stability (60 °C, 10 000 s, 1 MV cm^{-1}), (d) NBIS stability (0.5 mW cm^{-2} white light, 10 000 s, −1 MV cm^{-1}), and (e) NBTIS stability (60 °C, 0.5 mW cm^{-2} white light, 10 000 s, −1 MV cm^{-1}) of DGBC a-IGZO TFTs with an organic ILD layer between the substrate and the buffer oxide.

which was spin-coated and patterned *via* conventional photolithography. Because the ILD layer can withstand temperatures up to 230 °C, the μLEDs and oxide TFTs can be sufficiently integrated at this low temperature *via* monolithic fabrication. In order to prevent the diffusion of hydrogen and water vapor from ILD, an extra layer of T-ALD Al_2O_3 buffer oxide was applied.[47,55] Additional experiments were also conducted to explore the extent to which the ILD will affect the TFT performance; we deliberately omitted the ILD in the DGBC TFT structure.

Fig. S6 (ESI†) shows the TFT transfer, output curves, and stability (PBTS, NBIS, and NBTIS) of DGBC a-IGZO TFTs without the ILD layer; Fig. 5 illustrates the corresponding data for the device with the ILD layer. Comparing both results, the ILD did not degrade the TFT performance owing to the excellent barrier properties exhibited by the Al_2O_3 buffer layer.[47] In addition, Fig. S7–S11 (ESI†) depict the uniformity of device performance within a batch and between batches. The performance of devices was found to be highly consistent among testing samples from batch to batch regardless of the device location on the substrate. These results indicate that the monolithic fabrication reported in this article shows great reproducibility and reliability. Finally, we integrated DGBC TFT arrays on μLEDs *via* monolithic fabrication. Fig. 6(a and b) show the subpixel layouts of the μLED and TFT arrays and the FIB-SEM images of the sub-pixel surface, respectively. Remarkably, the device fabrication proceeded as designed. In

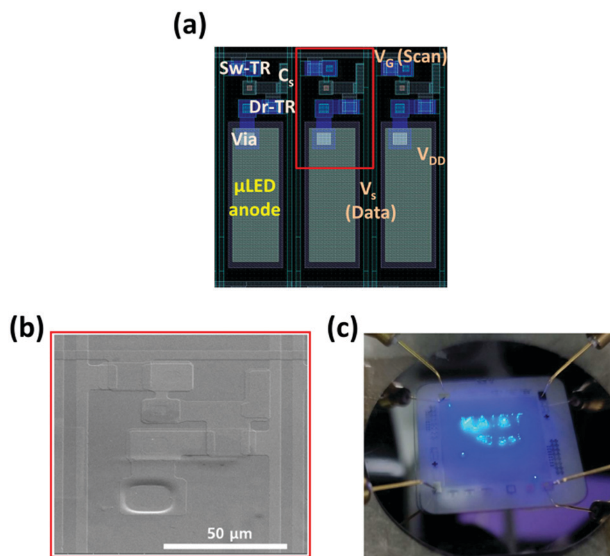

Fig. 6 (a) The subpixel layouts of the μLED and DGBC TFT arrays. (b) FIB-SEM image of the surface subpixels. (c) Image of the operation of μLED and DGBC TFT arrays when both of the arrays were turned on.

contrast to the existing inorganic ILD materials, which may contain numerous voids at low temperatures, our organic ILD (DW-10) processed by spin coating provides several merits such

This journal is © The Royal Society of Chemistry 2022

Open Access Article. Published on 27 June 2022. Downloaded on 2/20/2025 2:05:01 PM.
This article is licensed under a Creative Commons Attribution-NonCommercial 3.0 Unported Licence.

Table 1 Main set of achievements including our work and previous studies in the µLED field in terms of optoelectronics and microelectronics

Novelty	Driving devices	Integration method	LED	LED/driving circuit fabrication substrate	TFT structure	Bonding material	TFT process temperature	Year/ref.
Active-matrix (AM) driving: 8 × 8	PMOS	Flip-chip	GaN-µLED	Sapphire/silicon	—	Solder bump	—	2009/12
High-brightness (10^6 cd m^{-2})	CMOS	Flip-chip	GaN-µLED	Sapphire/silicon	—	Bump-bonded (Au)	—	2015/9
High-brightness (40 000 cd m^{-2}), AM driving	LTPS TFT	Flip-chip	GaN-µLED	Sapphire/glass	Conventional coplanar	Mo–Au layer	~450 °C	2018/17
2D materials (transparent conducting film/channel)	Graphene FET	Monolithic with the use of the graphene transfer method	GaN-µLED	Sapphire	Bottom-gate bottom-contact	No information	No information	2019/11
Large scale (12.1 inches), full-color	LTPS TFT	Mass transfer	µLED with color conversion materials	Glass	No information	No information	~450 °C	2019/19
Large scale (4 inches), full-color	a-IGZO TFT	Mass transfer	µLED	Glass	Conventional coplanar	Solder bump	No information	2020/24
Real-monolithic, highly-stable TFT (also AM driving)	a-IGZO TFT	Monolithic	GaN-µLED	Sapphire	Dual-gate	Organic inter-layer dielectric	Below 230 °C	This work

as rapid processability, inexpensive production cost, and no requirement for additional planarization.

Fig. 6(c) illustrates an operational image of the µLED driven by DGBC TFT arrays. The scan line was swept from −15 to 20 V to ensure the proper performance of the TFT array; the data line, V_{DD}, and V_{Ground} were 3.5, 5, and 0 V, respectively. As shown in Fig. 6(c), the phrase ''KAIST 70 ppi'' can be visualized, indicating that our unique methodology can achieve adequate monolithic fabrication of highly stable oxide TFTs on µLEDs under low temperature process conditions, compared to other previous achievements (Table 1). The thickness of the organic ILD on the µLEDs and unetched n-GaN was approximately 1.11 and 2.00 µm, respectively (Fig. S12, ESI†). This difference is considered reasonable as the µLED layer thickness is approximately 900 nm.

4 Conclusions

Our present study is the first to report reliable and low-temperature (below 230 °C) monolithic integration of active-matrix-µLED displays. A dual-gate a-IGZO TFT array controls the µLED displays to exhibit excellent electrical stability under the PBTS, NBIS, and NBTIS environments. In addition, this integration has been demonstrated to result in the development of superior TFTs, including reproducibility and reliability, which are crucial characteristics for future mass production in display technology. Comprehensive analyses of the electrical, structural, and chemical properties revealed that the deposited ALD-Al_2O_3 films had crucial roles in terms of high-quality dielectric properties and passivation of defects within the a-IGZO active layer/insulator interface by hydrogen. Our organic ILD ensures reliable interconnections by the excellent gap-filling and planarization properties, even at low temperatures, thus successfully creating the phrase ''KAIST 70 ppi'' from the active-matrix-µLED array. We believe that our method can be embedded in applications related to VR, AR, and biomedical sensors. Furthermore, in large-area high-resolution µLED displays, our novel monolithic method will be the cornerstone of mass production with low production costs.

Author contributions

Junghoon Yang: conceptualization, data curation, formal analysis, funding acquisition, visualization, validation, writing – original draft, and writing – review and editing. HyunWoo Park: investigation, methodology, software, and writing – original draft. Baul Kim: investigation and resources, Yong-Hoon Cho: conceptualization, writing – review and editing, and supervision. Sang-Hee Ko Park: project administration, supervision, and writing – review and editing.

Conflicts of interest

There are no conflicts to declare.

Acknowledgements

This work was supported by the National Research Foundation of Korea (NRF) grant from the Korean Government (no. 2020R1A6A3A13061266 and 2020M3E4A1080112) and by the Industry Technology R&D Program (20006476) funded by the Ministry of Trade, Industry, and Energy (MOTIE, Korea).

References

1 S. Jin, J. Li, J. Li, J. Lin and H. Jiang, *Appl. Phys. Lett.*, 2000, **76**, 631–633.
2 J. Yoon, S. M. Lee, D. Kang, M. A. Meitl, C. A. Bower and J. A. Rogers, *Adv. Opt. Mater.*, 2015, **3**, 1313–1335.
3 H. E. Lee, J. H. Shin, J. H. Park, S. K. Hong, S. H. Park, S. H. Lee, J. H. Lee, I. S. Kang and K. J. Lee, *Adv. Funct. Mater.*, 2019, **29**, 1808075.

Open Access Article. Published on 27 June 2022. Downloaded on 2/20/2025 2:05:01 PM.
This article is licensed under a Creative Commons Attribution-NonCommercial 3.0 Unported Licence.

4 Y. Huang, E.-L. Hsiang, M.-Y. Deng and S.-T. Wu, *Light: Sci. Appl.*, 2020, **9**, 1–16.

5 E. F. Schubert and J. K. Kim, *Science*, 2005, **308**, 1274–1278.

6 D. A. Gaul and W. S. Rees Jr, *Adv. Mater.*, 2000, **12**, 935–946.

7 L. Zhang, F. Ou, W. C. Chong, Y. Chen and Q. Li, *J. Soc. Inf. Disp.*, 2018, **26**, 137–145.

8 W. Meng, F. Xu, Z. Yu, T. Tao, L. Shao, L. Liu, T. Li, K. Wen, J. Wang and L. He, *Nat. Nanotechnol.*, 2021, **16**, 1231–1236.

9 J. Herrnsdorf, J. J. McKendry, S. Zhang, E. Xie, R. Ferreira, D. Massoubre, A. M. Zuhdi, R. K. Henderson, I. Underwood and S. Watson, *IEEE Trans. Electron Devices*, 2015, **62**, 1918–1925.

10 F. Templier, *J. Soc. Inf. Disp.*, 2016, **24**, 669–675.

11 Y. Fu, J. Sun, Z. Du, W. Guo, C. Yan, F. Xiong, L. Wang, Y. Dong, C. Xu and J. Deng, *Materials*, 2019, **12**, 428.

12 Z. J. Liu, K. M. Wong, C. W. Keung, C. W. Tang and K. M. Lau, *IEEE J. Sel. Top. Quantum Electron.*, 2009, **15**, 1298–1302.

13 E. Virey, *Inf. Disp.*, 2018, **34**, 22–27.

14 K. Tsuchiyama, K. Yamane, S. Utsunomiya, H. Sekiguchi, H. Okada and A. Wakahara, *Appl. Phys. Express*, 2016, **9**, 104101.

15 K. Myny, *Nat. Electron.*, 2018, **1**, 30–39.

16 Y. Sun, J. Fan, M. Liu, L. Zhang, B. Jiang, M. Zhang and X. Zhang, *J. Soc. Inf. Disp.*, 2020, **28**, 926–935.

17 H.-M. Kim, J. G. Um, S. Lee, D. Y. Jeong, Y. Jung, S. H. Lee, T. Jeong, J. Joo, J. Hur and J. H. Choi, *Dig. Tech. Pap. - Soc. Inf. Disp. Int. Symp.*, 2018, **49**, 880–883.

18 Z. Pan, C. Guo, X. Wang, J. Liu, R. Cao, Y. Gong, J. Wang, N. Liu, Z. Chen and L. Wang, *Adv. Mater. Technol.*, 2020, **5**, 2000549.

19 N. Sugiura, C.-T. Chuang, C.-T. Hsieh, C.-T. Wu, C.-Y. Tsai, C.-H. Lin, C.-C. Liu, C.-Y. Liu, C.-N. Yeh and C.-Y. Liu, *Dig. Tech. Pap. - Soc. Inf. Disp. Int. Symp.*, 2019, **50**, 450–453.

20 J. F. Wager, *Inf. Disp.*, 2014, **30**, 26–29.

21 J. F. Wager, *Inf. Disp.*, 2020, **36**, 9–13.

22 H. Yabuta, M. Sano, K. Abe, T. Aiba, T. Den, H. Kumomi, K. Nomura, T. Kamiya and H. Hosono, *Appl. Phys. Lett.*, 2006, **89**, 112123.

23 K. Nomura, H. Ohta, A. Takagi, T. Kamiya, M. Hirano and H. Hosono, *Nature*, 2004, **432**, 488–492.

24 Y. Sun, J. Fan, B. He, M. Zhang, S. Chen, X. Zhang, C.-E. Lee and Q. Fang, A Full-Color Micro LEDs Display Based on IGZO TFT, *2020 IEEE 3rd International Conference on Electronics Technology (ICET)*, 2020, pp. 46–49.

25 K. Nomura, T. Kamiya, H. Ohta, M. Hirano and H. Hosono, *Appl. Phys. Lett.*, 2008, **93**, 192107.

26 P. Barquinha, L. Pereira, G. Goncalves, R. Martins and E. Fortunato, *Electrochem. Solid-State Lett.*, 2008, **11**, H248.

27 A. Indluru and T. Alford, *Electrochem. Solid-State Lett.*, 2010, **13**, H464.

28 H.-W. Zan, W.-T. Chen, C.-W. Chou, C.-C. Tsai, C.-N. Huang and H.-W. Hsueh, *Electrochem. Solid-State Lett.*, 2010, **13**, H144.

29 R. Martins, D. Gaspar, M. J. Mendes, L. Pereira, J. Martins, P. Bahubalindruni, P. Barquinha and E. Fortunato, *Applied Materials Today*, 2018, **12**, 402–414.

30 Y. Nam, H.-O. Kim, S. H. Cho, C.-S. Hwang, T. Kim, S. Jeon and S.-H. Ko Park, *J. Inf. Disp.*, 2016, **17**, 65–71.

31 S. H. K. Park, D. H. Cho, C. S. Hwang, S. Yang, M. K. Ryu, C. W. Byun, S. M. Yoon, W. S. Cheong, K. I. Cho and J. H. Jeon, *ETRI J.*, 2009, **31**, 653–659.

32 T. Kamiya, K. Nomura and H. Hosono, *J. Disp. Technol.*, 2009, **5**, 468–483.

33 M. D. H. Chowdhury, J. G. Um and J. Jang, *Appl. Phys. Lett.*, 2014, **105**, 233504.

34 K. Ide, K. Nomura, H. Hiramatsu, T. Kamiya and H. Hosono, *J. Appl. Phys.*, 2012, **111**, 073513.

35 Y. Goh, J. Ahn, J. R. Lee, W. W. Park, S.-H. Ko Park and S. Jeon, *ACS Appl. Mater. Interfaces*, 2017, **9**, 36962–36970.

36 T. Kim, J.-H. Hur and S. Jeon, *Appl. Phys. Lett.*, 2015, **107**, 093503.

37 T. Kim, S. Park and S. Jeon, *Sci. Rep.*, 2017, **7**, 1–8.

38 M. Powell, C. Glasse, P. Green, I. French and I. Stemp, *IEEE Electron Device Lett.*, 2000, **21**, 104–106.

39 S. J. Yun, K.-H. Lee, J. Skarp, H.-R. Kim and K.-S. Nam, *J. Vac. Sci. Technol., A*, 1997, **15**, 2993–2997.

40 J. Kim, C. Fuentes-Hernandez, W. Potscavage Jr, X.-H. Zhang and B. Kippelen, *Appl. Phys. Lett.*, 2009, **94**, 142107.

41 H.-J. Jeong, K.-L. Han, K.-S. Jeong, S. Oh and J.-S. Park, *IEEE Electron Device Lett.*, 2018, **39**, 971–974.

42 D. Kim, H. Kang, J.-M. Kim and H. Kim, *Appl. Surf. Sci.*, 2011, **257**, 3776–3779.

43 K. Ide, Y. Kikuchi, K. Nomura, M. Kimura, T. Kamiya and H. Hosono, *Appl. Phys. Lett.*, 2011, **99**, 093507.

44 J. B. Ko, S.-H. Lee, K. W. Park and S.-H. K. Park, *RSC Adv.*, 2019, **9**, 36293–36300.

45 M. S. Oh, K. Lee, J. Song, B. H. Lee, M. M. Sung, D. Hwang and S. Im, *J. Electrochem. Soc.*, 2008, **155**, H1009.

46 Y. Nam, H.-O. Kim, S. H. Cho and S.-H. K. Park, *RSC Adv.*, 2018, **8**, 5622–5628.

47 Y. Kang, B. D. Ahn, J. H. Song, Y. G. Mo, H. H. Nahm, S. Han and J. K. Jeong, *Adv. Electron. Mater.*, 2015, **1**, 1400006.

48 M. Mativenga, S. Lim, F. Haque and J. Ryu, *Jpn. J. Appl. Phys.*, 2020, **59**, 104001.

49 J. Bang, S. Matsuishi and H. Hosono, *Appl. Phys. Lett.*, 2017, **110**, 232105.

50 K. W. Park, G. Jeon, S. Lee, J. B. Ko and S. H. K. Park, *Phys. Status Solidi A*, 2019, **216**, 1800737.

51 D. Kim, H. Park and B.-S. Bae, *AIP Adv.*, 2016, **6**, 035315.

52 J. Park, C. S. Kim, Y. S. Kim, Y. C. Park, H. J. Park, B.-S. Bae, J.-S. Park and H.-S. Kim, *J. Electroceram.*, 2016, **36**, 129–134.

53 M. Chun, M. D. H. Chowdhury and J. Jang, *AIP Adv.*, 2015, **5**, 057165.

54 J. Raja, K. Jang, H. H. Nguyen, T. T. Trinh, W. Choi and J. Yi, *Curr. Appl. Phys.*, 2013, **13**, 246–251.

55 K.-C. Ok, S. Oh, H.-J. Jeong, J. U. Bae and J.-S. Park, *IEEE Electron Device Lett.*, 2015, **36**, 917–919.

This journal is © The Royal Society of Chemistry 2022